PAPER

Visible spectroscopy of highly charged tungsten ions with the JET charge exchange diagnostic

Physica Scripta

PAPER

Visible spectroscopy of highly charged tungsten ions with the JET charge exchange diagnostic

Alex Thorman[1], Edward Litherland-Smith[1], Sheena Menmuir[1], Nick Hawkes[1], Martin O'Mullane[1], Ephrem Delabie[2], Bart Lomanowski[2], Josep Maria Fontdecaba[3], Shane Scully[1,*] and JET Contributors[4]

EUROfusion Consortium, JET, Culham Science Centre, Abingdon OX14 3DB, United Kingdom

[1] UKAEA/CCFE, Culham Science Centre, Abingdon, Oxon OX14 3DB, United Kingdom

[2] Oak Ridge National Laboratory, Oak Ridge, Tennessee 37831-6169, United states of America

[3] Laboratorio Nacional de Fusión, CIEMAT, 28080 Madrid, Spain

[4] See the author list of 'Overview of JET results for optimising ITER operation' by J. Mailloux *et al* to be published in Nuclear Fusion Special issue: Overview and Summary Papers from the 28th Fusion Energy Conference (Nice, France, 10-15 May 2021).

[*] Author to whom any correspondence should be addressed.

E-mail: shane.scully@ukaea.uk

Keywords: tungsten, charge exchange, magnetic dipole transition, visible spectroscopy, JET, ITER

RECEIVED
3 August 2021

REVISED
2 November 2021

ACCEPTED FOR PUBLICATION
10 November 2021

PUBLISHED
2 December 2021

Abstract

Since the installation of the ITER-like wall on the JET tokamak, visible emission from a broad range of tungsten charge states has complicated plasma ion temperature and toroidal rotation measurements. A plethora of charge exchange transitions, from ions up to W^{56+}, and 21 suspected magnetic dipole transitions have been observed. In particular W^{39+} and W^{46+} charge exchange emission contaminates the long-established carbon measurement at 529 nm. Fortunately the wavelength and relative intensity of the tungsten charge exchange lines is predictable and their influence can be mitigated when they are included in the spectral fit. Neon based charge exchange measurements at 525 nm are now preferred on JET since the ITER-like wall, however in this case an unidentified tungsten magnetic dipole transition contaminates the spectrum when the electron temperature is low.

1. Introduction

Magnetic confinement nuclear fusion is a candidate for future clean energy production. The JET tokamak holds the current record for the fusion energy 'gain' factor with $Q = 0.67$, while the next generation device ITER is designed to produce $Q \geqslant 10$. The plasma ion temperature is a critical factor in the calculation of the fusion power output and can be measured spectroscopically from atomic light emission. An understanding of all observed emission processes in the plasma is essential for both accurate measurements of the ion temperature and modelling of radiative losses from the plasma.

Charge exchange spectroscopy (CXS) is a mature visible spectroscopy diagnostic technique for measuring the ion temperature and rotation from Doppler broadened and shifted spectral lines [1, 2]. Traditionally tokamak walls have incorporated carbon based plasma facing components, giving rise to appreciable carbon concentrations in the plasma. The C VI $n = 8 \rightarrow 7$ 529nm transition, driven by charge exchange (CX) from the heating neutral beam, then provides a radially localised emission source from fully stripped ions. Other low Z ions such as H/D, He, Be, N, Ne and Ar have also been used for visible CXS [2, 3].

The walls in ITER will be made from tungsten and beryllium due to fears of tritium retention in carbon. Consequently an ITER-like wall (ILW) was also installed on the JET tokamak in 2011 [4]. Since the introduction of the ILW on JET, carbon CX measurements have become challenging due to:

- Reduced carbon concentrations leading to weaker emission intensity.
- Edge W I and W II nuisance emission lines polluting the carbon spectral region [5].

- W^{39+} and W^{46+} CX emissions overlapping with the carbon emission at moderate to high electron temperatures and tungsten densities.

When the core tungsten concentration is high, the newly identified tungsten CX transitions dominate the carbon CX emission and the edge tungsten nuisance lines. Several strategies have been developed at JET to overcome the shortcomings in the carbon measurements. Recently the CXS diagnostic on JET was upgraded to provide simultaneous dual view measurements from 3 different spectral regions, using 6 spectrometers to enhance the flexibility and reliability of the measurement [6]. Typically CX emission regions for carbon + neon, helium + beryllium and deuterium [7] are monitored. Neon is now regularly injected on JET and has become the most utilised impurity for measuring the ion temperature and rotation.

Tungsten (Z = 74) is only partially stripped of electrons at typical fusion electron temperatures and therefore radiative losses can be significant. A broad range of charge states are present in a JET plasma, with low charge ions in the edge to highly charged ions ($q \approx 60$) in the core. The majority of the power radiated from tungsten occurs at significantly higher frequencies than visible light, however visible transitions also exist. In section 2 visible tungsten CX transitions between high principal quantum number states are identified for the first time and their implications discussed. Then in section 3 the 21 suspected magnetic dipole transitions observed so far on JET are tabulated, with some newly observed and others that have been theoretically predicted [8, 9], observed on the LHD stellarator [10] or on electron beam ion trap (EBIT) devices [11, 12].

2. Active tungsten charge exchange

Visible tungsten transitions have been observed on JET following charge exchange interactions with neutral deuterium beam atoms described by,

$$D + W^{q+1} \rightarrow D^{+} + (W^{q})^{*} \tag{1}$$

where the W^q ion is excited to a level with high principal quantum number n. It is important to keep in mind that emission from W^q is reliant on the presence of the recombining ion W^{q+1}. The excited n level distributions for tungsten were extrapolated from a universal fit to low Z element cross sections, derived using the atomic-orbital close-coupling, unitarized distorted-wave approximation and classical trajectory Monte Carlo (CTMC) methods [13]. The most probable excitation level n_{max} for each charge state is shown in figure 1 and, as anticipated, the universal fit values lie 2-6 above the approximation $n_{max} \approx (q+1)^{3/4}$ [13, 14]. A more recent study for ITER relevant conditions applies two different CTMC methods directly to the recombination of W^{64+} [15]. The universal fit incorporates rCTMC calculations for argon and encouragingly the extrapolation produces similar results to the direct W^{64+} rCTMC calculations for JET relevant beam velocities (50—100 keV/amu).

The wavelengths of transitions between high n levels can be approximated by the familiar Rydberg formula. To more accurately predict the wavelength of the transitions, a recently devised relativistic Rydberg formula is used here given by [16, 17],

$$\frac{1}{n_{air}\lambda_{air}} = \frac{m_e c}{h}\left(\frac{1}{\sqrt{1-(q+1)^2\alpha^2/n_2^2}} - \frac{1}{\sqrt{1-(q+1)^2\alpha^2/n_1^2}}\right) \tag{2}$$

where α is the fine structure constant, c is the speed of light, h is Planck's constant, m_e the mass of the electron, n_{air} is the refractive index of air and (n_1,n_2) are the principal quantum numbers of the transition upper and lower levels respectively. The wavelength in air, λ_{air}, is used for the JET measurements presented here.

The regions of the JET spectrum most routinely observed for charge exchange spectroscopy are 460-478 nm containing He II 4 → 3 and Be IV 6 → 5 transitions, 520-535 nm containing C VI 8 → 7 and Ne X 11 → 10 transitions and 650-662 nm containing the D I 3 → 2 transition (Balmer-alpha) [6]. In table 1 tungsten charge exchange lines observed within the first two regions are compared with wavelength predictions from equation (2). The experimental values are mostly 0.01-0.04nm above the relativistic formula, with the most notable exceptions being the two $\Delta n = 2$ transitions which are just below the prediction. There is also a weak trend that the offset increases with q but this may simply be an artifact due to the uncertainties. As seen in figure 1, the upper levels for the observed $\Delta n = 1$ transitions are about 6-7 greater than the most probable for CX capture. Therefore emission rates for UV transitions (<200 nm) are expected to be greater than for these visible transitions, especially once subsequent cascades are taken into consideration.

The rest wavelengths listed in table 1 were established by comparing red and blue Doppler shifted wavelengths, measured from horizontally opposed tangential views of the JET neutral beams [6]. Doppler shifts of up to ~1nm are observed on JET due to the toroidal plasma rotation. A comparison with the neon rotation velocity is also possible, however rotation velocities for different species are known to be partially decoupled [18]. The force balance for species i, with the inclusion of centrifugal force is,

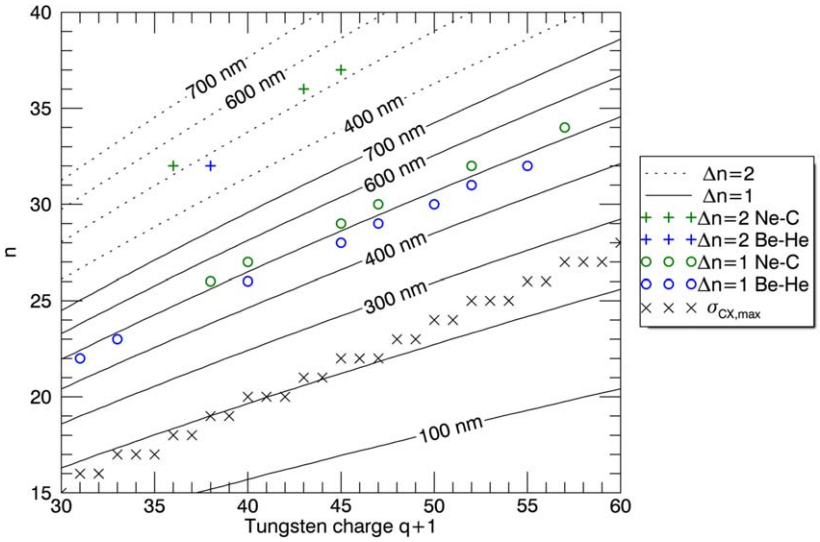

Figure 1. Contours showing the wavelength of $\Delta n = 1$ (solid) and $\Delta n = 2$ (dotted) transitions for a range of upper levels n and recombining charge states $q + 1$. Upper levels of the $\Delta n = 1$ (circles) and $\Delta n = 2$ (pluses) transitions observed on JET near 470 nm (blue) and 525 nm (green). (Black crosses) Most probable n_{max} level excited by a deuterium E = 70 keV/amu neutral beam.

$$\frac{-\nabla P_i}{n_i} + \frac{m_i v_{\phi,i}^2}{R}\hat{\mathbf{R}} + q_i e(\mathbf{E} + \mathbf{v}_i \times \mathbf{B}) = 0 \tag{3}$$

where e is the fundamental charge, P_i the pressure, n_i the species density and (R, ϕ, Z) cylindrical coordinates are used. The electric field is independent of the species and therefore can be factored out to compare the tungsten and neon (or other) rotation velocities. In the midplane the toroidal rotation for W^{q+1} is then,

$$v_{\phi,W} = v_{\phi,Ne} + \frac{k_B T}{eB_Z}\left(\frac{\frac{\partial n_W}{\partial R}}{(q+1)n_W} - \frac{\frac{\partial n_{Ne}}{\partial R}}{q_{Ne} n_{Ne}}\right) + \frac{k_B \frac{\partial T}{\partial R}}{eB_Z}\left(\frac{1}{q+1} - \frac{1}{q_{Ne}}\right)$$
$$- \frac{v_{\phi,Ne}^2}{eB_Z R}\left(\frac{m_W}{q+1} - \frac{m_{Ne}}{q_{Ne}}\right) + (v_{Z,W} - v_{Z,Ne})\frac{B_\phi}{B_Z}. \tag{4}$$

where k_B is the Boltzmann constant, $q_{Ne} = 10$ for neon and the approximation has been made for the centrifugal term that $|v_{\phi,W} - v_{\phi,Ne}| \ll |v_{\phi,Ne}|$. On JET the neutral beams rotate the plasma in the negative toroidal direction (co-current) and on the outboard side $B_Z > 0$ and $V_Z > 0$. In equation (4) the tungsten density gradient term, $(\partial n_W/\partial R)/n_W \sim 10\ \mathrm{m}^{-1}$, will typically dominate the fully stripped neon $(\partial n_{Ne}/\partial R)/n_{Ne}$ term due to sharp gradients in the tungsten charge state fractional abundance. On the cooler side of the W^{q+1} peak abundance the density gradient acts to increase the tungsten rotation (in the negative toroidal direction) while on the high temperature side it slows the tungsten rotation. Meanwhile the $\partial T/\partial R$ term contributes to slow the tungsten down relative to neon but this is somewhat counteracted by the centrifugal term. The centrifugal term can usually be discarded when comparing deuterium with carbon or neon as all have similar mass to charge ratios, however this is not the case with tungsten which has a higher mass to charge ratio. Finally, the poloidal rotation is usually the weakest term and tends to slow the tungsten relative to neon. Overall the net effect is that on the low temperature side of the peak abundance a rotation offset of $\Delta v_\phi \sim -10\ \mathrm{km\ s}^{-1}$ can exist, equivalent to $|\Delta\lambda| \approx 0.02$ nm. The offset crosses zero near the peak abundance before reaching $\Delta v_\phi \sim +20\ \mathrm{km\ s}^{-1}$ on the high temperature side, equivalent to $|\Delta\lambda| \approx 0.04$ nm.

A second complicating factor for the tungsten rotation velocity relates to viewing geometry effects and the sharp tungsten density gradients. The lines of sight pass through two banks of neutral beams, limiting the radial resolution to 3–17 cm [19], in addition to the 4cm diameter spot size for the observation volume. As a result, when observing on the low(high) temperature side of the charge state abundance peak the tungsten density and emission weighting will be biased more towards the core(edge) side, leading to a higher(lower) perceived rotation velocity. This effect is less apparent with standard low Z CX impurities as their ions are fully stripped and therefore have a relatively constant density. Overall this biased averaging effect and the force balance correction in equation (4) both contribute to increase the tungsten rotation on the low temperature side of the peak abundance and vice versa. This trend in the rotation offsets is noticeable in the JET measurements but is of comparable magnitude to the uncertainties in table 1.

Table 1. Visible tungsten CX transitions observed on JET between 465.5-478 nm and 520-530 nm. Lines with no quoted wavelength have been observed but are too close to nearby W CX lines to cleanly distinguish. Uncertainties, in round brackets, are estimated based on the transition intensity, the confidence in the Be II wavelength reference lines and the presence of any neighbouring lines.

JET (nm)	Relativisitc Rydberg (nm)	q + 1	$n_1 \rightarrow n_2$
466.00(3)	465.986	29	21 → 20
—	467.381	50	30 → 29
467.41(2)	467.398	45	28 → 27
468.86(3)	468.841	19	16 → 15
—	468.841	38	32 → 30
470.32(3)	470.301	55	32 → 31
470.505(20)	470.483	31	22 → 21
471.63(2)	471.602	40	26 → 25
475.92(2)	475.894	33	23 → 22
476.98(2)	476.948	47	29 → 28
477.62(4)	477.587	52	31 → 30
520.32(2)	520.296	45	29 → 28
522.39(2)	522.389	18	16 → 15
—	522.389	36	32 → 30
522.57(2)	522.561	38	26 → 25
523.865(20)	523.869	45	37 → 35
526.19(3)	526.146	52	32 → 31
526.75(5)	526.727	57	34 → 33
527.18(4)	527.194	43	36 → 34
528.99(2)	528.966	47	30 → 29
529.34(2)	529.327	40	27 → 26

When fitting the tungsten emission lines it is preferable to couple the rotation and temperature to the impurity CX measurements to limit the number of free parameters in the spectral fit and avoid the possibility of fitting to an undesired local minimum. Using a fixed wavelength offset is usually tolerable, but this ignores the rotation offsets in equation (4) and view biasing effect. More adaptive methods still need to be developed and implemented to properly account for these slight differences and improve the spectral fits.

2.1. Overlap of tungsten CX and impurity CX lines

Emission from W^{46+} (after recombination of W^{47+}) overlaps with the carbon CX emission as seen in figure 2. At first glance the W^{46+} emission could be confused with the carbon emission due to their similar rest wavelengths. However when the relatively narrow linewidth is compared with the neon line it becomes evident that the bulk of the emission Doppler shifted from 529 nm must come from a significantly heavier species like tungsten. Otherwise the carbon temperature would be badly underestimated if the W^{46+} emission were not included in the fit. A lower charge W^{39+} line also overlaps with the carbon CX emission, shown in figure 3. When bright, the W^{39+} emission is easier to distinguish from the carbon and would increase the inferred carbon wavelength if not included in the fit. W^{47+} and W^{40+} do not significantly overlap with each other, ignoring transport effects they peak in abundance at T_e=5.1 keV and 2.7 keV respectively [20]. Fortuitously the subsequent $\Delta n = 1$ cascades after W^{46+} 30 → 29 and W^{39+} 27 → 26 are both captured in the helium & beryllium portion of the spectrum, as seen in figure 1. These lower wavelength pairs are routinely observed on JET and assist in identifying cases where the contamination to the carbon measurement is considerable.

A number of lower charge state tungsten $\Delta n = 1$ CX lines also overlap with other commonly used impurity CX lines and their higher charge $\Delta n = 2$ counterparts also require consideration. For example the Be IV 6 → 5 CX emission at 465.86 nm overlaps with the W^{28+} 21 → 20 466.00 nm emission. In this case the peak fractional abundance of W^{29+} occurs at T_e=1.3 keV and is therefore only ever an issue at the very edge of the plasma. Its $\Delta n = 2$ counterpart, W^{57+} 42 → 40, is too weak to be noticeable in the JET core. The He II 4 → 3 CX emission at 468.57 nm is close to the W^{18+} 16 → 15 468.86 nm transition with a rare example later in figure 6. This tungsten line appears infrequently as its peak abundance is only 0.24 keV but weak hints of its $\Delta n = 2$ counterpart are more common. The Ne X 11 → 10 transition at 524.90 nm is near the W^{12+} 13 → 12 524.698 nm line however the temperature shell is too cold and narrow for the line to be readily observed. Potentially for such a low charge state passive excitation and emission from other impurities such as Ni^{12+} or Cu^{12+} are more likely.

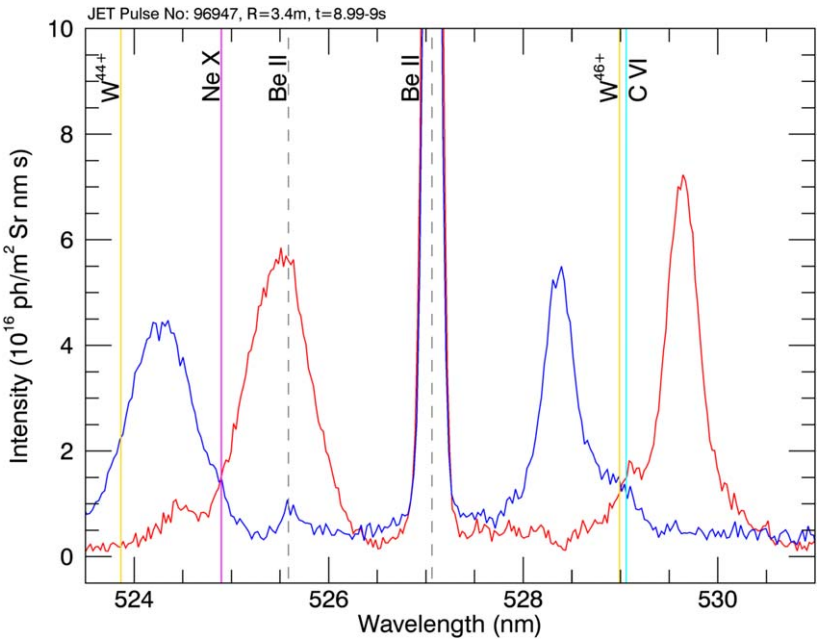

Figure 2. Red and blue Doppler shifted JET views of the carbon and neon CX region highlighting the W^{46+} emission with rest wavelength 528.99 nm (yellow) that dominates the 529.06 nm C VI emission (cyan). Ne X (magenta), Be II (grey dash) and the W^{44+} (yellow) emission rest wavelengths are also indicated.

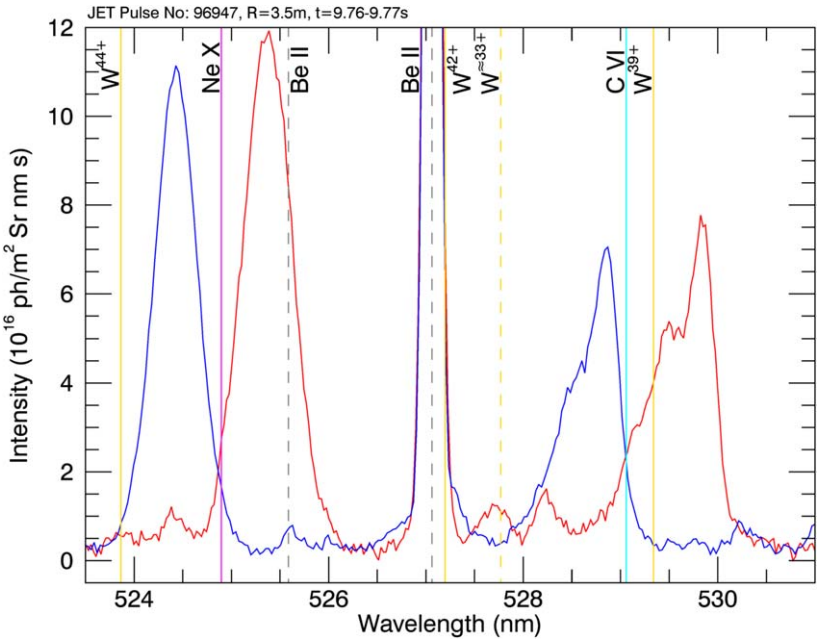

Figure 3. Red and blue shifted JET views of the carbon and neon CX region highlighting the W^{39+} emission with rest wavelength 529.34 nm (yellow) skewing the apparent position of the 529.06 nm C VI (cyan) to higher wavelengths. The W^{42+} & W^{44+} $\Delta n = 2$ transitions (yellow) and passive $W^{\approx 33+}$ (yellow dashed, see section 3) are also evident in the red shifted spectrum.

On the other end of the temperature scale it is worth noting the possibility of W^{65+} $36 \rightarrow 35$ 467.519 nm transition, with abundance peaking at $T_e = 34$ keV. This transition could be of interest on ITER if the He II $4 \rightarrow 3$ emission is used for CXS measurements, however it has not been observed on JET due to insufficient electron temperature and beam attenuation in the core would also be prohibitive.

2.2. LHD CX lines and Zeeman effect

A number of unidentified highly charged tungsten lines have previously been reported on LHD [10, 21–23]. After considering the JET identifications, it is now clear that several of these lines correspond to Rydberg

Table 2. Tungsten charge exchange lines observed on LHD that were previously unidentified.

Reported (nm)	Relativistic Rydberg (nm)	q + 1	$n_1 \rightarrow n_2$
389.91(4) [21, 22]	389.894	25	18 → 17
462.64 [10]	462.629	27	20 → 19
498.92 [10]	498.906	26	20 → 19
499.9 [10]	499.913	24	19 → 18
537.61 [10]	537.591	27	21 → 20
539.63 [10]	539.623	25	20 → 19
579.75 [10]	579.746	26	21 → 20
585.56 [10]	585.535	24	20 → 19
620.27 [10]	620.238	27	22 → 21
668.89 [10, 23]	668.873	26	22 → 21

transitions in the range W^{23-26+}, shown here in table 2. All of the wavelengths lie 0-0.03nm above the prediction from the relativistic Rydberg equation, a similar range to the 0.01-0.04 nm offsets observed on JET in table 1. In the 450-715 nm range studied by Shinohara *et al* [10] only 4 of the 13 possible $\Delta n = 1$ CX lines are not listed, namely W^{24+} 19 → 18 460.7 nm, W^{24+} 21 → 20 627.1 nm, W^{23+} 21 → 20 680.4 nm and W^{26+} 23 → 22 710.9 nm. It appears the 10-O port used for the LHD observations views two of the three LHD neutral beams, hence the excitation mechanism is also anticipated to be charge exchange.

Polarisation resolved measurements of the 669 nm line on LHD, that we believe to be the W^{25+} 22 → 21 transition, revealed Zeeman splitting with g-factor of 0.94 ± 0.04 [23]. The g-factor of 1 expected for hydrogenic transitions is 1.5 uncertainty intervals from the LHD measurement. The tungsten CX transitions on JET also exhibit some additional broadening however they are yet to be observed with sufficient resolution. Some additional broadening from the fine structure should also not be ruled out.

Typically for low mass CX transitions such as deuterium, carbon and neon the thermal broadening dominates the Zeeman splitting, while the instrumental function is accounted for in the fitting routine. However the Zeeman splitting is more noticeable in the case of tungsten as the higher mass reduces the thermal contribution to the linewidth. To understand the effect on the overall linewidth, the π-σ Zeeman splitting is given by,

$$\Delta\lambda_B = g\frac{eB\lambda_0^2}{4\pi m_e c}. \tag{5}$$

The two σ wings each have an intensity proportional to $1 + \cos^2\psi$ and the central π component $2\sin^2\psi$, where ψ is the angle between the magnetic field (B) and line of sight. Each of the three Zeeman components will be Doppler broadened with $1/e$ width given by,

$$\Delta\lambda = \sqrt{\frac{2kT}{m_i c^2}}\lambda_0. \tag{6}$$

Therefore in the absence of other broadening mechanisms $T \propto \Delta\lambda^2$, however when both the Zeeman effect and Doppler broadening are considered the approximate width is found to be,

$$\Delta\lambda_{net}^2 = \Delta\lambda^2\left[1 + (1 + \cos^2\psi)\frac{\Delta\lambda_B^2}{\Delta\lambda^2} + \left(2 - \frac{5\sin^2\psi}{2} + \frac{3\sin^4\psi}{4}\right)\frac{\Delta\lambda_B^4}{\Delta\lambda^4} + \ldots\right] \tag{7}$$

when $\Delta\lambda_B \ll \Delta\lambda$. Essentially the linewidth of a single fitted Gaussian is no longer a direct measurement of the temperature. The inferred temperature, when neglecting the Zeeman effect, would be overestimated by the factor given in the square brackets.

The inferred temperatures of deuterium, carbon, neon and tungsten are shown in figure 4 for a simulation fitting a single Gaussian to the combined σ and π emission and are consistent with approximation in equation (7). For the correction to be 1%, that is $\Delta\lambda_B \approx 0.1\Delta\lambda$, only requires a temperature of 1 keV for deuterium, a justification for why it is often ignored. Meanwhile for neon it is only reached at 10 keV and for tungsten it is never satisfied as it requires 93 keV. The $\Delta\lambda_B^2/\Delta\lambda^2$ term in equation (7) scales with m_i hence the correction is linear with mass in most cases. However for tungsten, even at moderate temperatures, the $\Delta\lambda_B^4/\Delta\lambda^4$ term is also significant such that the correction for tungsten can be over 10 × greater than for neon. For the moment we are fitting a single Gaussian to the tungsten lines, coupled with a rescaled width relative to

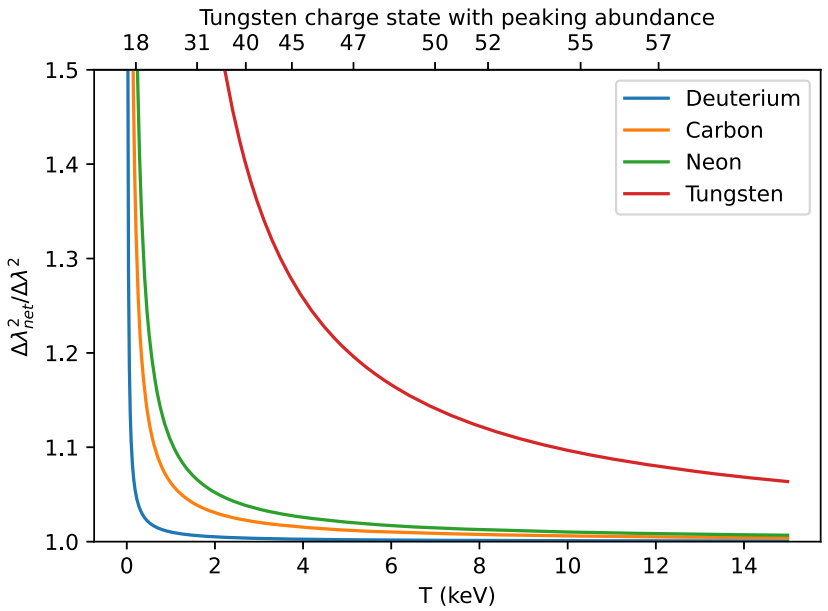

Figure 4. Correction factor ($\Delta\lambda^2_{net}/\Delta\lambda^2$) needed to account for the contribution of Zeeman splitting on the linewidth. Typical JET parameters of $B = 3$ T, $\psi \approx 0$ and $\lambda_0 = 525$ nm are used, leading to a Zeeman splitting of $\Delta\lambda_B = 0.04$ nm. The top axis shows the temperature of the fractional abundance peak for several tungsten charge states assuming that $T_i = T_e$.

the neon temperature, however a three Gaussian fit for the σ and π components will be more appropriate in the future.

3. Passive tungsten magnetic dipole transitions.

Electric dipole (E1) emission, from transitions between lower levels of highly charged tungsten, occurs at frequencies much higher than visible light. However visible emission from magnetic dipole (M1) transitions between highly populated low energy sub-levels are also possible. The first laboratory observation of these visible tungsten 'forbidden lines' was conducted on an electron beam ion trap (EBIT) where 3 W^{26+} transitions were detected, along with accompanying theoretical modelling [8]. Since then many other transitions from varying tungsten charge states have been observed, with the majority of the measurements below 505 nm.

21 passive tungsten emission lines have so far been observed on JET, thought to derive from tungsten magnetic dipole transitions. These transitions are listed in table 3 and where possible are linked to existing EBIT and LHD measurements as well as theoretical models. The wavelength scan is not comprehensive as the measurements have been made parasitically. Additionally the occurrence of the lines is often irregular and multiple shots are desirable to confirm their intensity correlates with the routinely surveyed 464.62 nm W^{26+} transition. The most scrutiny was placed on the 460-475 nm and 520-532 nm regions but particular effort was also made to observe the 389 nm & 502 nm W^{26+}, 494 nm & 588 nm W^{25+}, 510 nm $W^{\approx 27+}$ [10] and 607nm W^{28+} transitions. 527.61 nm W^{11+} [24] and 527.74 nm W^{13+} [25] transitions lie in the most scrutinised region of the JET measurements but have not been observed suggesting they are relatively weak. The majority of the lines observed on JET have a charge in the range $q = 24 - 28$, with the corresponding peak abundance occurring at relatively low temperatures of $T_e \sim 1$ keV. Anomalous conditions are therefore required to observe the transitions, initially requiring high confinement to establish a significant tungsten concentration but then also a low temperature gradient to maximise the width of the emission region.

Tungsten charge exchange transitions were also regularly observed when tuning the spectrometer to look for magnetic dipole transitions but fortunately their location can be reliably predicted from equation (2). Additionally, the nature of the emission lines on JET was verified by comparing active channels looking directly through the neutral beams and passive 'off beam' channels, as well as comparing the temporal correlation of the line intensity with the neutral beam power. Special consideration was also given before classifying some of the passive lines, for example the 521.8 nm line is at a similar wavelength to the 521.812 nm W^{22+} $24 \rightarrow 22$ transition and the 524.72 nm line to the 524.698 nm W^{12+} $13 \rightarrow 12$ & W^{25+} $26 \rightarrow 24$ transitions. The only line observed on LHD [10] not included in tables 2 or 3 is the 509.11nm line. A weak line at 509.04(5)nm was observed on JET and is attributed to the W^{27+} $27 \rightarrow 25$ 509.029 nm line. The 0.07 nm offset between the LHD

Table 3. Rest wavelengths of the passive tungsten emission observed on JET, compared with LHD, EBIT and theoretical values from various sources. Effort has been made to convert experimental wavelengths to air, but theoretical wavelengths are transcribed directly as they tend to have lower accuracy. Uncertainties, where given, are in round brackets and for JET are estimated based on the line intensity, the confidence in the wavelength reference line(s) and the presence of other nearby obscuring lines. The relative photon emissivity has been calculated for transitions of nearby charge after factoring in fractional abundances. A separate emissivity scaling is necessary for the suspected W^{5+} emission regime, highlighted by the *.

JET (nm)	LHD (nm)	EBIT (nm)	Theory (nm)	q	Suspected Transition	Relative Emissivity
389.39(3)	389.37(4) [21]	389.41(6) [8] 389.35(3) [26] 389.433(12) [27]	388.4 [8] 390.9 [27] 389.7 [28] 390.8 [29]	26	$^3H_5 \rightarrow {}^3H_4$	1.5
393.05(3)	—	393.06(6) [11] 392.99(3) [26] 393.09(3) [30]	399.01 [30]	28	$(5/2,5/2)_3 \rightarrow (5/2,5/2)_2$	0.13
394.46(3)	—	394.41(3) [26]	—	30(1)	—	0.18
464.62(2)	—	464.68(6) [8, 11] 464.64(15) [27]	467.8 [8] 464.7 [27] 463.9 [28] 464.4 [29]	26	$^3H_6 \rightarrow {}^3H_5$	1
467.76(5)	—	467.80(6) [11]	—	24	—	0.04
468.17(5)	—	468.22(6) [11]	—	24	—	0.04
469.07(4)	—	469.21(6) [11] 469 [12]	469.7 [31] 470.3 [29]	25	$^4G_{5/2} \rightarrow {}^4F_{3/2}$	0.16
471.15(3)	—	471.18(6) [11]	—	24	—	0.10
493.6(1)	493.6 [10]	493.62(6) [11] 493.70(15) [31] 494 [12]	492.33 [31] 499.2 [29]	25	$^4I_{11/2} \rightarrow {}^4I_{9/2}$	0.6
501.97(3)	501.99 [10]	501.99(6) [8] 502.15(17) [27]	501.8 [8] 505.6 [27] 501.9 [28] 503.1 [29]	26	$^3F_3 \rightarrow {}^3F_2$	0.5
509.77(5)	509.81 [10]	—	—	27(1)	—	0.2
513.83(3)	—	—	516.0 [8] 507.1 [27] 505.6 [28] 508.5 [29]	26(1)	$^3P_2 \rightarrow {}^3P_1$	0.1
521.80(3)	—	522.0 [12, 32]	518.3 [31] 538.1 [29]	25	$^4P_{3/2} \rightarrow {}^4F_{3/2}$	0.08
523.59(2)	—	—	—	26(1)	—	0.06
524.18(2)	—	—	—	5(2)	—	0.5*
524.72(3)	—	—	—	26(1)	—	0.14
527.49(1)	—	—	—	5(2)	—	1*
527.77(3)	—	—	513.2 [33] 526.6 [34]	33(1)	$^2I_{13/2} \rightarrow {}^2I_{11/2}$	0.04
581.20(5)	—	581 [12]	585.1 [29]	25	$^4G_{7/2} \rightarrow {}^2F_{5/2}$	0.1
587.63(4)	—	587.5(2) [31] 588 [12]	587.71 [31] 588.4 [29]	25	$^4I_{13/2} \rightarrow {}^4I_{11/2}$	0.35
607.48(2)	—	—	605.57 [30]	28	$(5/2,7/2)_6 \rightarrow (5/2,5/2)_5$	0.35

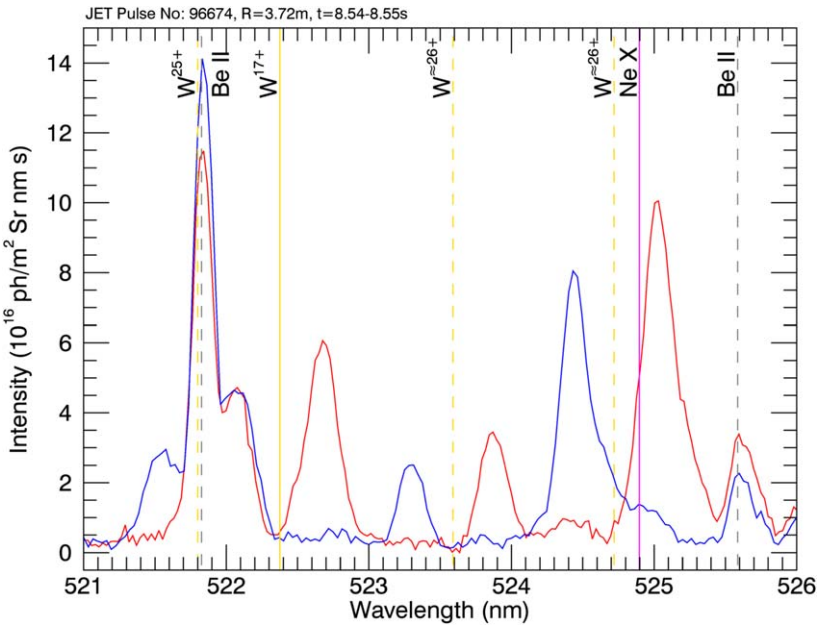

Figure 5. Red and blue shifted views of the neon CX region of the JET spectra with low edge temperature and high tungsten concentration. Neon was not seeded for the shot hence the neon peak is very weak. Dashed lines represent the rest wavelength of passive transitions and solid lines active CX transitions for tungsten (yellow), beryllium (grey) and neon (magenta).

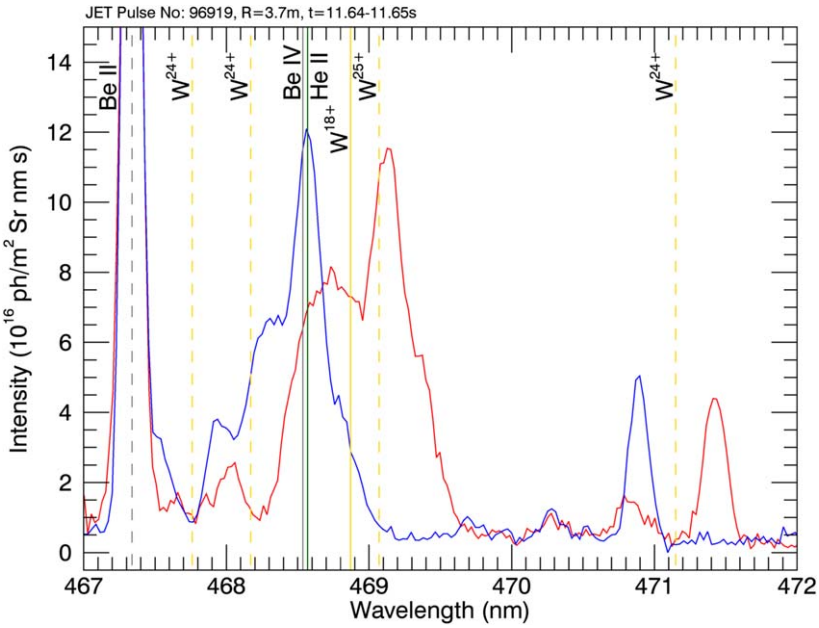

Figure 6. Red and blue shifted views of the He II 4 → 3 and Be IV 8 → 6 region with low edge temperature and high tungsten concentration. Dashed lines represent the rest wavelength of passive transitions and solid lines active CX transitions for tungsten (yellow), beryllium (grey) and helium (green).

and JET measurements is larger than the offsets seen in tables 1 and 2, hence the source of this line on LHD is unclear.

The charge states reported in table 3 are the values most consistent with the JET measurements but have also been informed by the existing literature. Conceivably three different properties of the emission line could be used to measure the charge state, namely the line intensity profile, the Doppler shift and the line broadening. The spatio-temporal evolution of the line intensity was found to be the simplest and most reliable method. The intensity profile for each charge state can be predicted from the line integral $\int n_e^2 A(q,\ T_e)\, dl$, where $A(q, T_e)$ is the fractional abundance [20] for a given charge state and electron temperature, while it is assumed that the tungsten concentration and photon emissivity coefficient are uniform and constant. A particularly useful scenario is when

a high performance pulse rapidly drops core electron temperature resulting in a temporal cascade through decreasing tungsten charge states. For typical JET conditions the $q = 24 - 28$ magnetic dipole lines Doppler shift roughly 0.3 nm. While we had some success modelling the Doppler shift, the reliance on additional experimental inputs (i.e. the relatively sparse rotation profile) to the model tended to make it less accurate in differentiating between charge states. Finally, the linewidths measured are larger than predicted from pure Doppler broadening and it is suspected other broadening mechanisms contribute to the linewidth. For example, the 581.2 nm W^{25+} line appears to be broader than the 587.63 nm W^{25+} line. Overall EBIT measurements of the charge state, relying on a comparison of the electron energy and tungsten ionisation energy, appear to be a more accurate method than the measurements on JET.

A mixture of horizontal and vertical channels were used to help measure the wavelengths reported in table 3. The vertical channels with minimal Doppler shift are particularly useful as they don't require any comparison to a forward model. That said, in some cases the Doppler shift in the horizontal channels is beneficial, for example blue shifting of the 464.62 nm W^{26+} line helped to distinguish it from a bright C III multiplet which may have obscured it on LHD.

The identification of some transitions in table 3 is speculative and some justifications are given here. The ground configuration of W^{26+} only has 13 levels and the W^{26+} $^3P_2 \rightarrow {}^3P_1$ line is the only magnetic dipole transition with a predicted wavelength near the 513.83 nm, 523.59 nm and 524.72 nm lines. The 513.83 nm line appears to be the most likely candidate based on the theoretical wavelength predictions. The JET observations are suggestive that $q > 25$ for the remaining 523.59 nm and 524.72 nm lines, especially when their neighbouring 521.8 nm W^{25+} transition appears to be a reliable reference point. However no other appropriate candidate W^{26+} ground configuration transitions exist. Only one W^{27+} ground configuration transition exists at 337.8 nm and none of the transitions predicted within the first excited configuration of W^{27+} [35] are close in wavelength or have been observed on LHD [10] or EBITs [11]. Therefore the charge states for the 523.59 nm and 524.72 nm lines remains a mystery. Similarly for the 509.77 nm line no W^{26-28+} candidates appear in the literature, nevertheless the JET measurements are suggestive that $q > 26$ after comparison with its well established neighbouring W^{26+} 501.97 nm transition.

We have favoured transitions between lower levels when attempting to identify the W^{25+} transitions. This approach is more compelling when some additional linkages are made within the existing literature that suggest many of the low lying transitions have already been observed. For example, EBIT measurements by Murata *et al* [12] found bright 687nm and 731 nm W^{25+} lines that we note are consistent with the $^4I_{15/2} \rightarrow {}^2I_{13/2}$ (688.1 nm [31] & 681.8 nm [29]) and $^2F_{5/2} \rightarrow {}^4F_{3/2}$ (727.5nm [31] & 731.1 nm [29]) transitions respectively. Meanwhile the 44 059 $\pm$ 25cm^{-1} (226.90 $\pm$ 0.13 nm) $^4H_{9/2} \rightarrow {}^4I_{9/2}$ and 20 249 $\pm$ 6 cm^{-1} (493.70 $\pm$ 0.15nm) $^4I_{11/2} \rightarrow {}^4I_{9/2}$ lines observed by Li *et al* [31] imply that the $^4H_{9/2} \rightarrow {}^2I_{11/2}$ transition is 23 809 $\pm$ 26cm^{-1} (419.89 $\pm$ 0.45 nm). The branching fractions suggest the $^4H_{9/2} \rightarrow {}^2I_{11/2}$ transition is 6.7 $\times$ less intense than the $^4H_{9/2} \rightarrow {}^4I_{9/2}$ transition [29] and is therefore still likely to be observable. The reasonably bright 421.28 $\pm$ 0.06nm line reported by Komatsu *et al* [11] is the only nearby candidate and although this would require 3$\times$the uncertainty to be consistent it appears to be the most plausible explanation.

The identification of the three W^{24+} transitions is too ambiguous to speculate. It seems likely one of them is the $^1L_8 \rightarrow {}^5I_8$ transition predicted at 462.3 nm [29] and possibly another is the $^3L_9 \rightarrow {}^1L_8$ transition predicted at 470.1nm [36]. The 394.4 nm W^{30+} line seen on JET and with an EBIT [26] could potentially be the transition predicted at 374.7nm [33] but the EBIT measurement of a 1.5$\times$ brighter 376.54(3)nm [26] appears to be a more likely candidate for that transition. A candidate for the 527.77nm line seen on JET (figure 3) is suggested in table 3 but the level of confidence is low given the charge state is uncertain. The two suspected W^{5+} lines have very weak Doppler shifts and occur infrequently, requiring very low temperatures. An example of these lines appears in figure 2 of [5] and studies similar to that on W^{5-7+} [37] may help to identify these transitions.

3.1. Overlap of tungsten M1 and impurity CX lines

The 524.72 nm tungsten line, shown in figure 5, interferes with neon ion temperature measurements on JET. Typically, during NBI heating the passive tungsten lines seen in the figure are not noticeable, but at times when the edge temperature gradient is weak they can become bright. Fortunately coupling the wavelength, apparent temperature and relative intensity of the 523.59 nm and 524.72 nm transitions assists the spectral fit to distinguish the 524.72 nm line from the neon CX line. This is particularly useful towards the core, where often the drop off in neon CX intensity with beam attenuation is greater than that for the passive tungsten emission. A theoretical candidate or EBIT experimental confirmation of the charge state of these two transitions would be beneficial to confirm the validity of this approach.

The standard helium CX emission line is also affected by tungsten lines at very low temperatures, with an example in figure 6. The 468.17 nm and 469.07 nm magnetic dipole transitions along with the W^{18+} 16 $\rightarrow$ 15 CX transition make the fit particularly troublesome, however like in the neon case these line only become

problematic in the presence of atypically low edge temperatures under 1 keV. The 468.17 nm and 469.07 nm lines are not easily distinguishable from the intrinsic beryllium emission and their identification was greatly assisted by the Komatsu *et al* EBIT measurements [11].

4. Conclusion

Three types of tungsten transitions have now been shown to complicate the JET CX measurements, namely W and W^{1+} E1 transition [5], charge exchange transitions and magnetic dipole transitions. The realisation of the highly charged tungsten transitions has been greatly assisted by the recent upgrades to the CXS diagnostic [6]. It is expected that these tungsten emission lines will also be present in the ITER spectrum and on other machines with tungsten plasma facing components. A vast range of these tungsten transitions exist and adaptive fitting regimes are necessary to optimise the constraints on the spectral fit.

The discovery of the W^{39+} and W^{46+} CX lines further highlights the challenges faced with carbon CX spectra on JET since the installation of the ILW. Fortunately, the W CX transitions are straightforward to predict. On the other hand, tungsten magnetic dipole emission also affects the neon and helium CX spectra but only when the edge temperature is unusually low. Unfortunately, these transitions are less straightforward to predict and understand but atomic modelling and experimental EBIT measurements have proved useful for finding and identifying many of the magnetic dipole lines on JET. For example the possible identification of the 607.48 nm W^{28+} line was based on modelling [30], whilst the 521.8nm W^{25+} line was greatly assisted by EBIT measurements [12]. Several new suspected tungsten magnetic dipole lines are also reported on JET, we hope these transitions can be identified by further modelling and EBIT measurements, in particular the 524.72 nm line that occasionally interferes with the neon CX emission.

In theory the tungsten CX emission could be used for ion temperature and rotation measurements but given the unreliability of the tungsten concentration and the narrow spatial range of each charge state it would not work routinely. One positive aspect is that newly identified tungsten CX transitions will allow us to diagnose spatially and charge resolved tungsten concentrations. Further work will include studies of the tungsten density and transport, requiring benchmarking of tungsten density measurements against other diagnostics along with benchmarking of the cross section calculations. Additionally improvements to the spectral fitting constraints on JET will further reduce the impact of the tungsten lines on the standard CX measurements by fully incorporating the rotation offsets and Zeeman splitting.

Acknowledgments

This work has been carried out within the framework of the EUROfusion Consortium and has received funding from the Euratom research and training programme 2014-2018 and 2019-2020 under grant agreement No 633 053 and from the RCUK [grant number EP/T012250/1]. The views and opinions expressed herein do not necessarily reflect those of the European Commission.'

Data availability statement

All data that support the findings of this study are included within the article (and any supplementary files).

ORCID iDs

Alex Thorman https://orcid.org/0000-0001-5912-9325
Martin O'Mullane https://orcid.org/0000-0002-2160-4546
Ephrem Delabie https://orcid.org/0000-0001-9834-874X
Josep Maria Fontdecaba https://orcid.org/0000-0001-7678-0240

References

[1] Isler R C 1994 *Plasma Phys. Controlled Fusion* **36** 171–208
[2] von Hellermann M G *et al* 2005 *Phys. Scr.* T **120** 19–29
[3] Whyte D G, Isler R C, Wade M R, Schultz D R, Krstic P S, Hung C C and West W P 1998 *Phys. Plasmas* **5** 3694–9
[4] Matthews G F *et al* 2011 *Phys. Scr.* **T145** 014001
[5] Menmuir S, Giroud C, Biewer T M, Coffey I H, Delabie E, Hawkes N C, Sertoli M and (JET EDDA Contributors) 2014 *Rev. Sci. Instrum.* **85** 11E412
[6] Hawkes N C, Delabie E, Menmuir S, Giroud C, Meigs A G, Conway N J, Biewer T M and Hillis D L 2018 *Rev. Sci. Instrum.* **89** 10D113

[7] Lomanowski B, Delabie E, Thorman A, Menmuir S, Litherland-Smith E, Biewer T and Klepper C 2019 Main ion charge exchange spectroscopy on JET in preparation for the DT campaign *LXI Annual Meeting of the APS Division of Plasma Physics* vol 64 *(Fort Lauderdale, Florida)* (American Physical Society) http://meetings.aps.org/link/BAPS.2019.DPP.UO8.1
[8] Ding X B, Koike F, Murakami I, Kato D, Sakaue H A, Dong C Z, Nakamura N, Komatsu A and Sakoda J 2011 *J. Phys. B: At. Mol. Opt. Phys.* **44** 145004
[9] Qiu M L, Li W X, Zhao Z Z, Yang Y, Xiao J, Brage T, Hutton R and Zou Y 2015 *J. Phys. B: At. Mol. Opt. Phys.* **48** 144029
[10] Shinohara M, Fujii K, Kato D, Nakamura N, Goto M, Morita S and Hasuo M 2015 *Phys. Scr.* **90** 125402
[11] Komatsu A, Sakoda J, Minoshima M, Sakaue H A, Ding X B, Kato D, Murakami I, Koike F and Nakamura N 2012 *Plasma and Fusion Research* **7** 1201158
[12] Murata S, Safronova M S, Safronova U I and Nakamura N 2020 *X-Ray Spectrom.* **49** 200–3
[13] Foster A 2008 On the behaviour and radiating properties of heavy elements in fusion plasmas *Phd Thesis* The University of Strathclyde https://www.adas.ac.uk/theses/foster_thesis.pdf
[14] Olson R E 1981 *Phys. Rev.* A **24** 1726–33
[15] Ralchenko Y and Schultz D R 2019 *Plasma Phys. Controlled Fusion* **61** 125007
[16] Suto K 2020 *Journal of Modern Physics* **11** 294–303
[17] Haug E G 2020 *Journal of Modern Physics* **11** 528–34
[18] Baylor L R, Burrell K H, Groebner R J, Houlberg W A, Ernst D P, Murakami M and Wade M R 2004 *Phys. Plasmas* **11** 3100
[19] Giroud C, Meigs A G, Negus C R, Zastrow K D, Biewer T M, Versloot T W and (Contributors J E) 2008 *Rev. Sci. Instrum.* **79** 10F525
[20] Summers H P 2004 The ADAS User Manual, version 2.6 www.adas.ac.uk
[21] Kato D *et al* 2013 *Phys. Scr.* T **156** 014081
[22] Morita S *et al* 2013 *AIP Conf. Proc.* **1545** 143–52
[23] Fujii K, Takahashi Y, Nakai Y, Kato D, Goto M, Morita S and Hasuo M 2015 *Phys. Scr.* **90** 125403
[24] Li M, Qiu M, Xiao J, Yao K, Brage T, Hutton R and Zou Y 2016 *Phys. Scr.* **91** 105401
[25] Zhao Z Z, Qiu M L, Zhao R F, Li W X, Guo X L, Xiao J, Chen C Y, Zou Y and Hutton R 2015 *J. Phys. B: At. Mol. Opt. Phys.* **48** 115004
[26] Watanabe H, Nakamura N, Kato D, Sakaue H A and Ohtani S 2012 *Can. J. Phys.* **90** 497–501
[27] Fei Z, Li W, Grumer J, Shi Z, Zhao R, Brage T, Huldt S, Yao K, Hutton R and Zou Y 2014 *Physical Review A—Atomic, Molecular, and Optical Physics* **90** 052517
[28] Ding X, Liu J, Koike F, Murakami I, Kato D, Sakaue H A, Nakamura N and Dong C 2016 *Phys. Lett.* A **380** 874–7
[29] Safronova U I, Safronova M S and Nakamura N 2017 *Phys. Rev.* A **95** 042510
[30] Qiu M L, Zhao R F, Guo X L, Zhao Z Z, Li W X, Du S Y, Xiao J, Yao K, Chen C Y, Hutton R and Zou Y 2014 *J. Phys. B: At. Mol. Opt. Phys.* **47** 175002
[31] Li W, Xiao J, Shi Z, Fei Z, Zhao R, Brage T, Huldt S, Hutton R and Zou Y 2016 *J. Phys. B: At. Mol. Opt. Phys.* **49** 105002
[32] Nakamura N 2020 *Private Communication*
[33] Jonauskas V, Gaigalas G and Kučas S 2012 *At. Data Nucl. Data Tables* **98** 19–42
[34] Karpuškien R and Kisielius R 2019 *At. Data Nucl. Data Tables* **125** 287–312
[35] Ding X, Murakami I, Kato D, Sakaue A H, Koike F and Dong C 2012 *Plasma and Fusion Research* **7** 2403128
[36] Gaigalas G, Rynkun P, Alkauskas A and Rudzikas Z R 2012 *At. Data Nucl. Data Tables* **98** 391–436
[37] Lu Q *et al* 2019 *Phys. Rev.* A **99** 042510